Supplementary Information

Regulating the Crystallization of Mixed-Halide Perovskites by Cation Alloying for Perovskite-Organic Tandem Solar Cells

Mingqian Chen,[ad] Yanxun Li,[ad] Zixin Zeng,[a] Ming Liu,[ad] Tao Du,[c] Xiaofeng Huang,[bd] Leyu Bi,[bd] Jiarong Wang,[ad] Wenlin Jiang,[bd] Yidan An,[ad] Sai-Wing Tsang,[ad] Jun Yin,*[c] Shengfan Wu*[ade] and Alex K.-Y. Jen*[abdf]

a. Department of Materials Science & Engineering, City University of Hong Kong, Kowloon, Hong Kong, 999077, China

b. Department of Chemistry, City University of Hong Kong, Kowloon, Hong Kong, 999077, China

c. Department of Applied Physics, The Hong Kong Polytechnic University, Kowloon, Hong Kong, 999077, China

d. Hong Kong Institute for Clean Energy, City University of Hong Kong, Kowloon, Hong Kong, 999077, China

e. School of Interdisciplinary Studies, Lingnan University, Tuen Mun, Hong Kong, 999077, China

f. State Key Laboratory of Marine Pollution, City University of Hong Kong, Kowloon, Hong Kong 999077, China

† Electronic supplementary information (ESI) available.

*Email: jun.yin@polyu.edu.hk; shengfanwu@ln.edu.hk; alexjen@cityu.edu.hk

Keywords: wide-bandgap perovskite, solar cells, alloy structure, crystallization, energy losses

Supplementary Note 1: Calculation of lattice strain.

The doped concentration of different ligands is 2 mol%.

The Williamson-Hall plots are devoted to calculating the residual strain derived from the XRD patterns in both 2D perovskite films using the following equation:

$$\beta cos\theta = \varepsilon(4sin\theta) + K\lambda/D \quad (1)$$

where β stands for the total broadening of XRD peaks, defined as full width at half maximum (FWHM), θ represents the diffraction angle, Ɛ is the residual strain, K refers to the Scherer constant (around 0.9 for perovskite), λ is the X-ray wavelength (1.542 Å), and D is the average crystal size of the film[1].

Supplementary Note 2: The carrier lifetime analysis from TRPL curves.

The TRPL curves of the corresponding perovskite films were fitted using a biexponential decay function equation:[1]

$$y = A_1 \exp\left(\frac{-t}{\tau_1}\right) + A_2 \exp\left(\frac{-t}{\tau_2}\right) + y_0 \quad (2)$$

where A_1 and A_2 are the relative amplitudes, τ_1 and τ_2 are the PL decay times for the fast and slow charge recombination, respectively[2].

Supplementary Note 3: Calculation of Urbach energy (E_u)**.**

The E_u of the 2D RP perovskite films was calculated from UV-Vis absorption spectra using the following equation:

$$a = a_0 \, exp\left(\frac{E - E_g}{E_u}\right) \quad (3)$$

where α is the absorption coefficient, E refers to the low photon energy range, and E_g represents the bandgap[3].

Supplementary Note 4: The detailed analysis of various losses in the wide-bandgap PSC.

To gain deeper insights into the sources of photovoltage loss, we calculated the energy loss ($e\Delta V$) of the control and target PSCs according to detailed balance theory, which can be expressed as $E_g - qVoc = e\Delta V = (e\Delta V_1 + e\Delta V_2 + e\Delta V_3)$, where ΔV_1 is originated from the black-body radiation and the non-ideal EQE above E_g, ΔV_2 is ascribed to the energy loss associated with extra thermal radiation in a cell where EQE of PSC extend into the region below E_g, and ΔV_3 results from the non-radiative recombination in the device (Figure S12). The details of the calculation can be found in our previous work.[3]

Supplementary note 5: The additional experimental details of organic sub-cells and challenges for the PO-TSCs.

In the context of PO-TSCs, the choice of a hole-transport layer for the organic sub-cell is a critical consideration. Thermally evaporated molybdenum oxide (MoO_x) stands out as an excellent option, primarily due to its compatibility with the underlying perovskite sub-cell and its ability to offer favorable electrical and optical properties. In this study, we have determined that a thickness of 10 nm represents the optimal value for MoO_x. Deviating from this thickness, either in the direction of thicker or thinner films, results in reduced optical transmittance or compromised electrical properties. Notably, we have also identified that a low evaporation rate, specifically 0.05 Å s^{-1}, improves the film quality of MoO_x, consequently contributing to higher device efficiency. In this work, the weight ratio of PM6:BTP-eC9:$PC_{71}BM$ in a ternary blend of 1:1:0.2 yielded superior results. It is worth highlighting that in the case of PNDIT-F3N, its limited solubility in methanol necessitated the addition of 0.5 vol% of acetic acid to aid in its dissolution. Importantly, we stress that the incorporation of acetic acid should be conducted outside of a glovebox during organic solar cell fabrication due to the potential influence of its vapor on device performance.

Experimental

Materials

Cesium iodide (CsI), formamidinium iodide (FAI) and formamidinium bromide (FABr) were purchased from Dysol. Lead iodide (PbI_2, purity of 99.999%), lead bromide ($PbBr_2$, purity of 99.9%) and 1-chloronaphthalene (1-CN) were purchased from TCI. Lead chloride ($PbCl_2$), imidazole iodide (IAI), methylammonium chloride (MACl), fullerene (C_{60}) and BCP (purity of 99.9%) were purchased from Xi'an Polymer Light Technology Corporation. DMF (purity of 99.99%), DMSO (purity of 99.50%), IPA (purity of 99.50%) and chlorobenzene (CB, purity of 99.90%) were purchased from J&K and used as received. PM6 and BTP-eC9 were purchased from Organtec Ltd. $PC_{71}BM$ was purchased from American Dye Source, Inc. Molybdenum oxide (MoOx), chloroform (CF, purity of 99.90%) and methanol (MeOH, purity of 99.90%) were purchased from Sigma-Aldrich. The gold and silver pellets for thermal evaporation use were purchased from ZhongNuo Advanced Material (Beijing) Technology Co.) with high purity. The (7H-dibenzo[c,g]carbazole) phosphonic acid (CbzNaph, hole-selective SAM) and piperazinium iodide (PI, surface-passivating agent for perovskite) were synthesized as reported in our previous studies.

Preparation of the perovskite precursor solution

To prepare wide-bandgap perovskite precursor ($Cs_{0.2}FA_{0.8}Pb(I_{0.6}Br_{0.4})_3$) with a concentration of 1.2 M, CsI (0.144 M), CsBr (0.096 M), FAI (0.576 M), FABr (0.384 M), PbI_2 (0.756 M) and $PbBr_2$ (0.48 M) were dissolved in 1 ml of mixed DMF/DMSO solvent (vol/vol, 4:1). It should be noted that 3.0 mol% of $MAPbCl_3$ was added. For the target devices, 2 mol% of the IA was added to the perovskite precursor. The solutions were stirred overnight at room temperature, and no filtration was required before use.

Preparation of the solution for the organic BHJ layer

To prepare the precursor for the organic active layer (BHJ layer), PM6, BTP-eC9 and $PC_{71}BM$ with a weight ratio of 1:1:0.2 were dissolved in CF, and the concentration of PM6 was fixed at 8 mg ml^{-1}. The solvent additive (0.5 vol%) (DIO) was added to the solution, which

was then stirred at 40 °C for 2 h before use.

Fabrication of single-junction wide-bandgap PSCs

The pre-patterned ITO glass substrates were sequentially cleaned by sonication with detergent (Decon 90/deionized water with 1:1/vol: vol), deionized water, acetone and IPA for 15 min, respectively. The cleaned ITO glass substrates were then transferred into an oven at 100 °C for 24 h and treated with O_2 plasma for 10 min before use. The CbzNaph hole-selective SAM (0.75 mg ml^{-1} in IPA) was spin-coated onto ITO glass substrates at 3,000 r.p.m. (with a ramping rate of 2,000 r.p.m. s^{-1}) for 25 s, and subsequently annealed at 110 °C for 15 min. After cooling, the substrates were rinsed with IPA solvent and annealed for another 5 min at 100 °C. The perovskite film was then deposited on the CbzNaph layer by a one-step spin-coating method. Specifically, 50 μl of the perovskite precursor was spin-coated at 500 r.p.m. for 4 s, then 4000–6500 r.p.m. (with a ramping rate of 1,500 r.p.m. s^{-1}) for 30 s. During the spin-coating process, 200 μl of CB anti-solvent was quickly dripped onto the centre of the perovskite film 10 s before the end of the process and then annealed at 100 °C for 15 min. Next, PI (0.3 mg ml^{-1} in IPA) was dynamically spin-coated onto the as-formed perovskite at 5,000 r.p.m. for 30 s, followed by annealing at 100 °C for 10 min. All the above spin-coating processes were conducted in an N_2-filled glovebox with the contents of O_2 and H_2O < 5 ppm at a controlled temperature of ~20 °C. Finally, 20-nm C_{60}, 6-nm BCP (or 10-nm SnO_2) and 100-nm Ag were thermally evaporated in a high-vacuum chamber (<2 × 10^{-6} torr) through a metal shadow mask (aperture area, 0.042 cm^2), then 100 nm MgF_2 was thermally evaporated onto the glass side of the devices as an antireflection (AR) layer.

Fabrication of single-junction narrow-bandgap organic solar cells (OSCs)

OSCs with a p–i–n configuration were based on the device structure of glass/ITO/MoO_x/PM6:BTP-eC9:$PC_{71}BM$/PNDIT-F3N/Ag. First, 10 nm MoO_x was thermally evaporated (at a rate of 0.05 Å s^{-1}) on clean ITO substrates in a high-vacuum chamber (<6 × 10^{-7} torr). Then, PM6:BTP-eC9:$PC_{71}BM$ solution was dynamically cast onto the MoO_x layer at 2,500 r.p.m. for 40 s and followed by thermal annealing at 90 °C for 10 min. After cooling, a PNDIT-F3N (0.5 mg ml^{-1} in methanol with 0.5 vol% of acetic acid) interfacial layer was

dynamically spin-coated onto the organic BHJ layer at 1,500 r.p.m. for 30 s. Finally, 100-nm Ag was thermally evaporated in a high-vacuum chamber (<2 × 10^{-6} torr) through a metal shadow mask.

Fabrication of the monolithic PO-TSCs (two-terminal configuration)

PO-TSCs described in this study, the narrow-bandgap organic subcells were integrated on top of the perovskite subcells. Briefly, after thermal evaporation of BCP in wide-bandgap subcells, 0.5-nm Au (at a rate of 0.05 Å s^{-1}) and 10-nm MoO_x were thermally evaporated on top of the BCP, respectively, to form an ICL structure for the tandem cells. The organic BHJ layer and interfacial layer were then sequentially spin-coated on MoO_x. PNDIT-F3N was dynamically spin-coated on the organic BHJ layer at 1,500 r.p.m. for 40 s. Finally, 100-nm Ag was thermally evaporated through a metal shadow mask.

Density functional theory (DFT) calculations

For the molecular calculations, the molecular geometries were optimized using ωB97XD functional with 6-31+G(d,p) basis set for H, C, N, O, S atoms and LANL2DZ for Pb and I atoms. All the molecular calculations were performed using the Gaussian09 program (D. 01). The binding energies for DMSO/PbX_2 and DMSO-PbX_2/IA were calculated as

$$E_{\mathrm{DMSO/PbX2}}\,(\mathrm{binding}) = E\,(\mathrm{DMSO/PbX_2}) - E\,(\mathrm{DMSO}) - E\,(\mathrm{PbX_2})$$

$$E_{\mathrm{DMSO\text{-}PbX2/IA}}\,(\mathrm{binding}) = E\,(\mathrm{DMSO\text{-}PbX_2/IA}) - E\,(\mathrm{DMSO\text{-}PbX_2}) - E\,(\mathrm{IA})$$

where E (DMSO/PbX_2) is the total energy of DMSO/PbX_2, E (DMSO-PbX_2/IA) is the total energy of DMSO-PbX_2/IA; E (DSMO), E (PbX_2), E (DMSO-PbX_2), and E (IA) are the energies of isolated DMSO molecule, PbI_2 cluster, DMSO-PbX_2 cluster, and IA molecule, respectively. For the periodic crystal calculations, the crystal structures were optimized using the projector-augmented wave (PAW) method as provided by the Vienna Ab initio Simulation Package (VASP). The generalized gradient approximation (GGA) with the Perdew-Burke-Ernzerhof (PBE) exchange-correlation functional was used. The van der Waals (vdW) interactions were also included in the calculations using the zero-damping DFT-D3 method of Grimme. A uniform grid of 6×6×6 *k*-mesh in the Brillouin zone was employed to optimize the crystal structures of cubic-phase $FAPbI_3$ in bulk, 4×4×1 *k*-mesh for $FAPbI_3$ slabs, and 2×2×1 *k*-mesh

for IA-passivated $FAPbI_3$. The 3×3 $FAPbI_3$ supercells, containing four or five octahedral layers, were exposed (100) surfaces with both FAI-rich and PbI_2-rich terminations, as well as a surface iodine interstitial (I_i). The slab replicas were separated by ~20 Å of vacuum. The energy cutoffs of the wavefunctions were set at 500 eV for the bulk and 450 eV for the slabs and interfaces. Each crystal structure was optimized until forces on single atoms were less than 0.015 eV/Å. The binding energies between $FAPbI_3$ and IA were calculated as

$$E_{IA/FAPbI3}\,(\text{binding}) = E\,(IA/FAPbI_3) - E\,(IA) - E\,(FAPbI_3)$$

where E ($IA/FAPbI_3$) is the total energy for IA passivated $FAPbI_3$; E (IA) and E ($FAPbI_3$) are the energies of isolated IA molecule and $FAPbI_3$ supercell, respectively.

Characterizations

^{1}H NMR spectra were measured on Bruker AVANCE III 300-MHz and 400-MHz spectrometers. Solution UV–vis absorption spectra were obtained using an Agilent 8454 spectrophotometer. Cyclic voltammetry measurements were conducted on a CHI660D electrochemical workstation. Transmittance and absorption spectra were conducted on a UV–vis spectrometer (PE Lamda 750). tdPL spectra were collected using a home-built facility, where an excitation laser (450 nm) was introduced to the sample through a fiber, and the PL spectra were detected using a detector connected to an Ocean Optics USB2000 spectrometer. XPS was performed on a Thermo Fisher ESCALAB XI + X-ray photoelectron spectrometer. Non-monochromatic He I was used as UV light with an energy of 21.2 eV. The top-viewing morphology of the thin-film samples and cross-sectional profile of the tandem cell were conducted by SEM (QUATTRO S). Powder and thin-film XRD characterizations were conducted on a D2 Phaser instrument with Cu Kα (wavelength of 1.5418 Å) radiation. In situ PL spectra were characterized with home-built equipment. An excitation laser (315 nm) was introduced to the sample through a fibre, and the PL spectra were detected by using a detector connected to an Ocean Optics USB2000. PL mapping was collected using a WITec alpha300 M+ confocal microscope. The excitation laser was a diode-pumped solid-state laser (532 nm, Cobolt Laser).

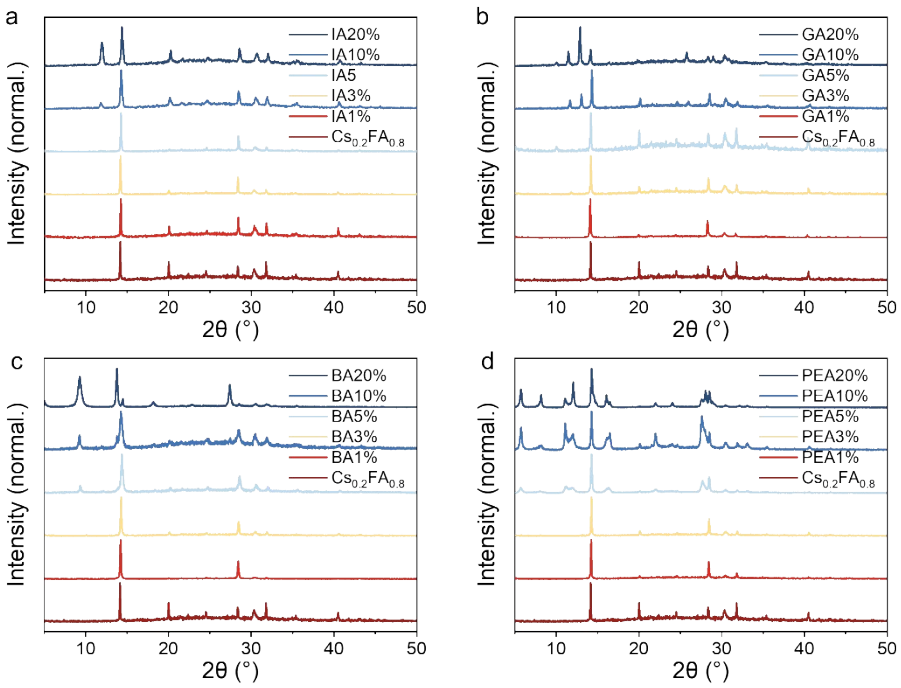

Figure S1. XRD pattern of cation-doped films with varying contents based on $Cs_{0.2}FA_{0.8}(I_{0.6}Br_{0.4})_3$-system.

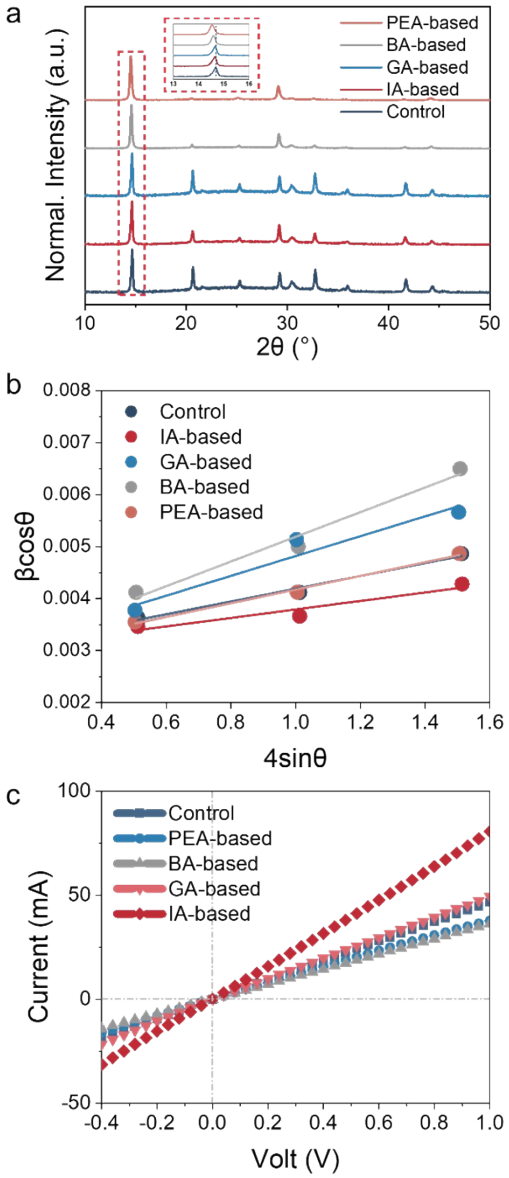

Figure S2. (a) Normalized XRD pattern of cation-doped (2 mol%) films, (b) the corresponding Williamson–Hall plots and fitting results, and (c) Linear *I–V* characteristics of the corresponding perovskite films in the dark with device configuration of ITO/perovskite/Ag.

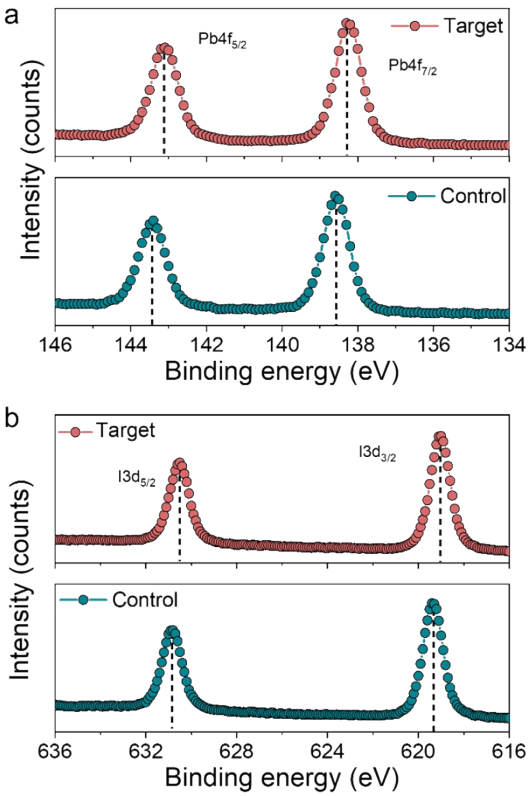

Figure S3. (a) Pb 4f and (b) I 3d XPS spectra of the control and target films.

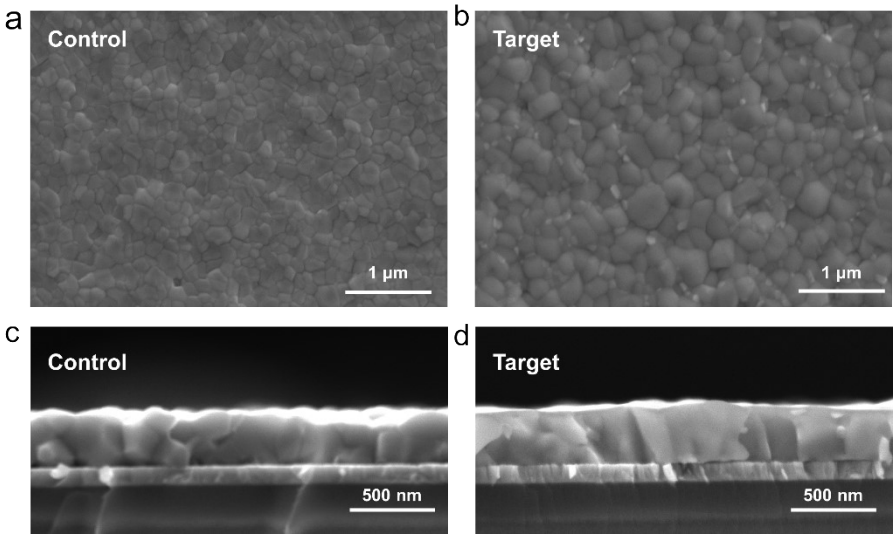

Figure S4. SEM and cross-sectional images of (a, c) control and (b, d) target films.

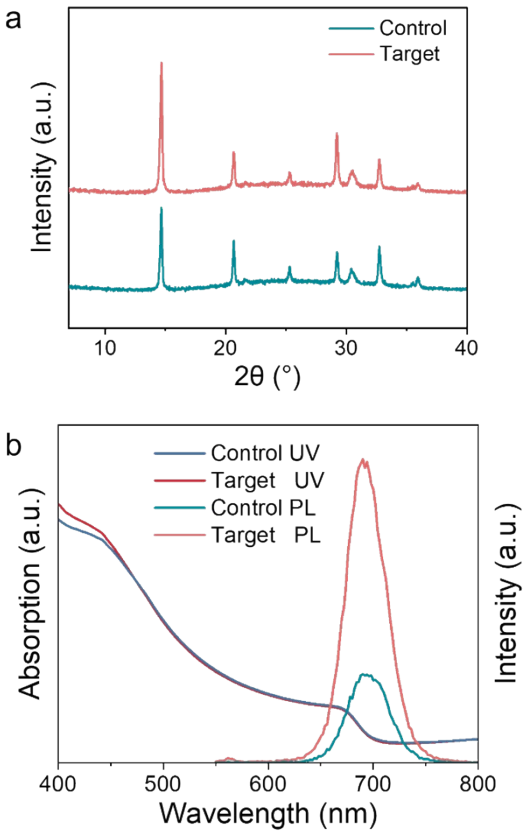

Figure S5. (a) XRD pattern of control and target perovskite film and (b) UV-vis and photoluminescence (PL) spectrometry of corresponding films.

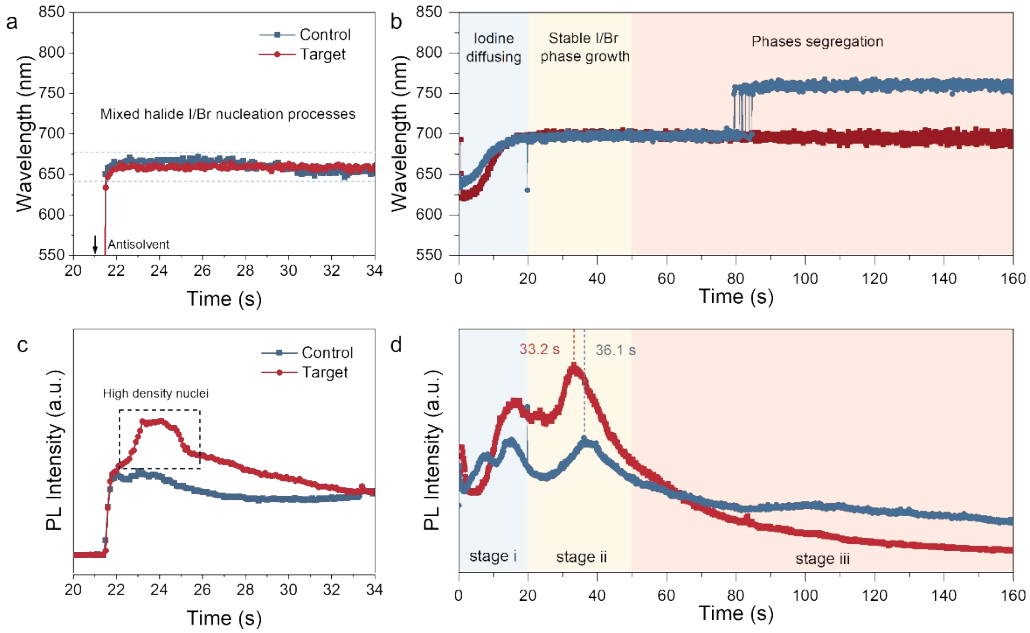

Figure S6. The in situ PL evolution for corresponding perovskite films is shown: (a, b) the tracking of the PL peak position and (c, d) its corresponding PL intensity as a function of time.

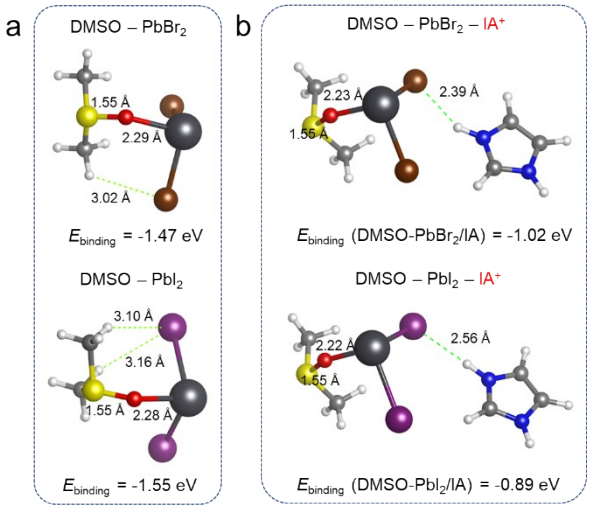

Figure S7. Molecular structures, atomic distances (dashed green lines), and binding energies ($E_{binding}$) between (a) solvent DMSO and PbX_2 and between (b) DMSO-PbX_2 and IA.

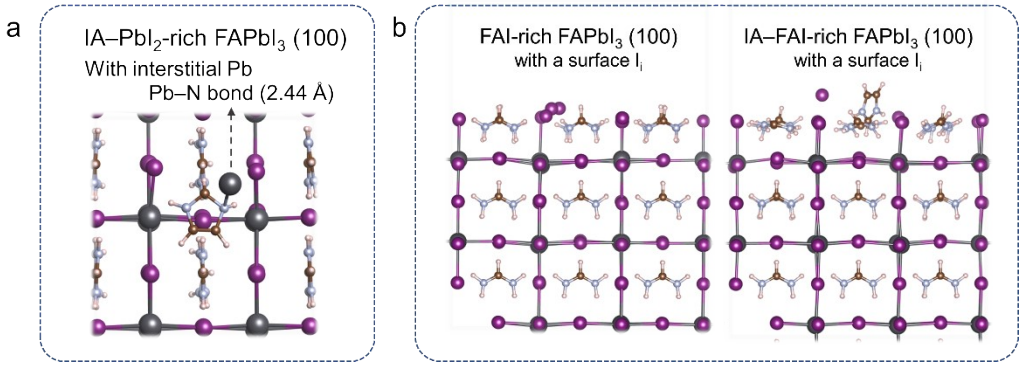

Figure S8. (a) PbI_2-rich $FAPbI_3$ (100) with a surface lead interstitial (Pb_i) exhibits coordination interaction with IA and (b) FAI-rich $FAPbI_3$ (100) with a surface iodide interstitial (I_i) before and after IA passivation.

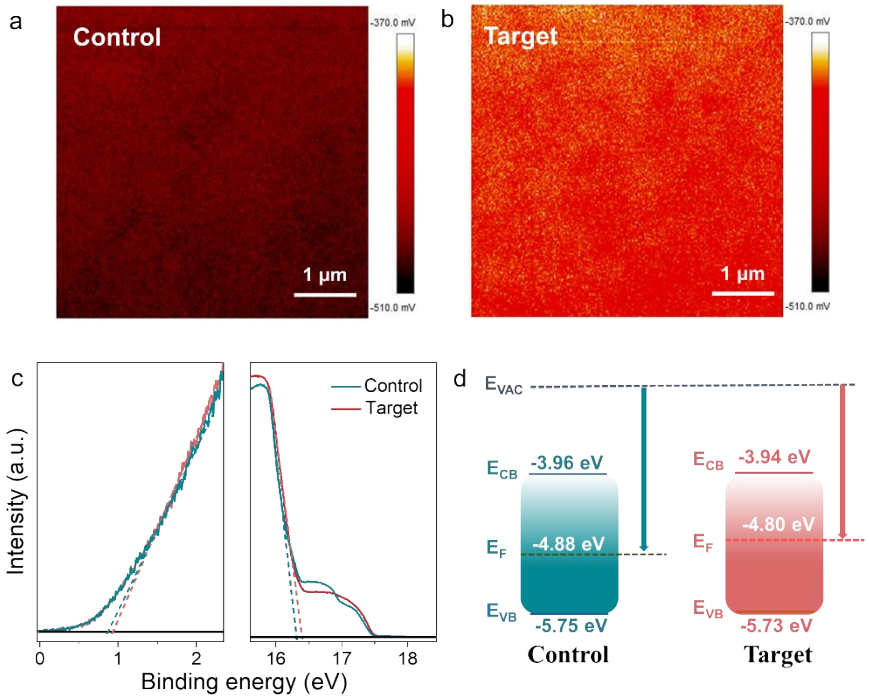

Figure S9. Kelvin probe force microscopy (KPFM) images of the (a) control and (b) target perovskite films. (c) UPS spectra of corresponding films. (d) Schematic energy level diagrams of the corresponding perovskite films.

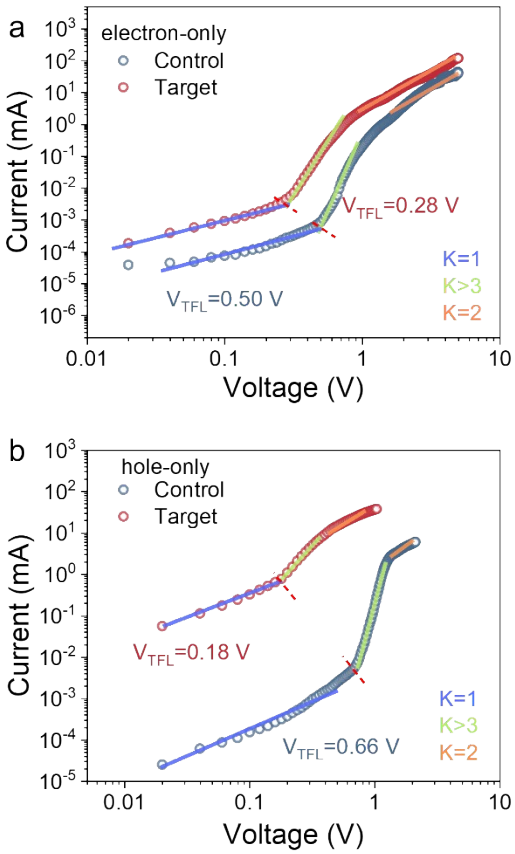

Figure S10 *J-V* curves for the electron-only devices with a glass/ITO/PCBM/perovskite/C_{60}/Ag structure (a), for the hole-only devices with a glass/ITO/SAM/perovskite/MoOx/Ag structure (b); The kink points of V_{TFL} were used for estimating trap-state density from the ohmic current to trap-filling current and electron mobility in respective conditions.

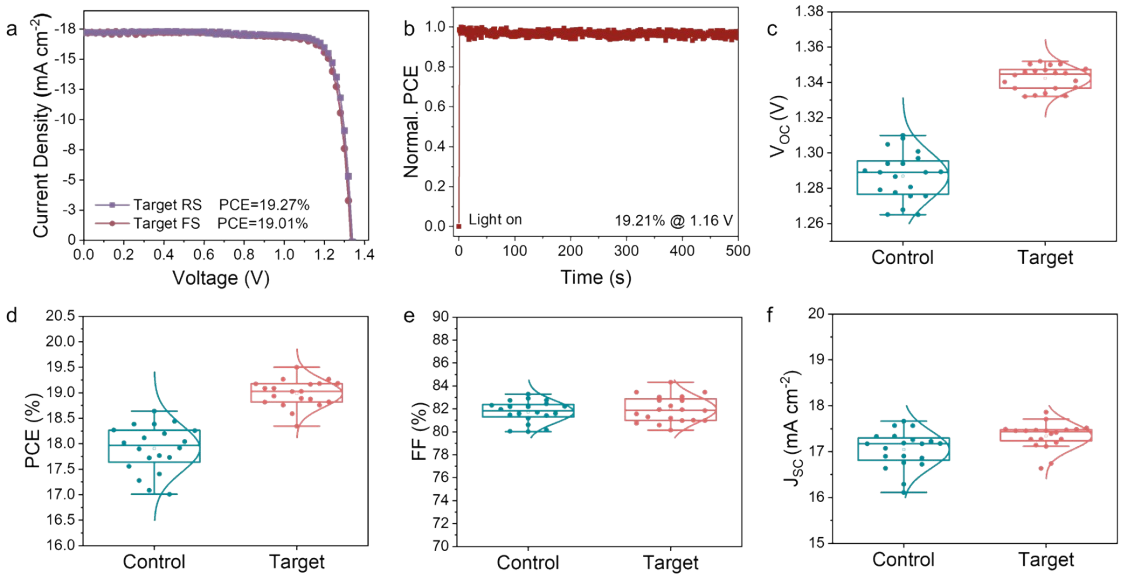

Figure S11. (a) The forward and reverse bias scanned *J-V* characteristics of the IA-alloyed device (b) Stabilized power output of the IA-based device. Statistical(c) V_{OC}, (d) PCE, (e) FF, and (f) J_{SC} of the corresponding devices were obtained from 20 individual devices.

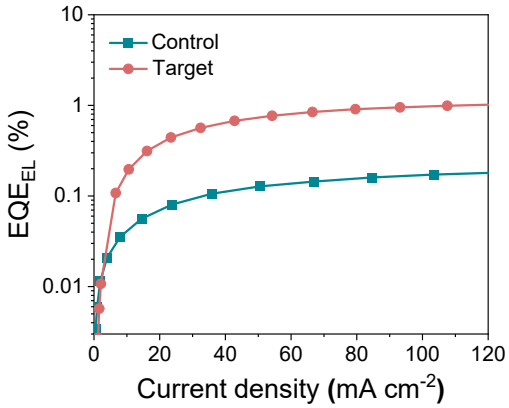

Figure S12. The electroluminescence external quantum efficiency (EQE_{EL}) of the control and target PSC.

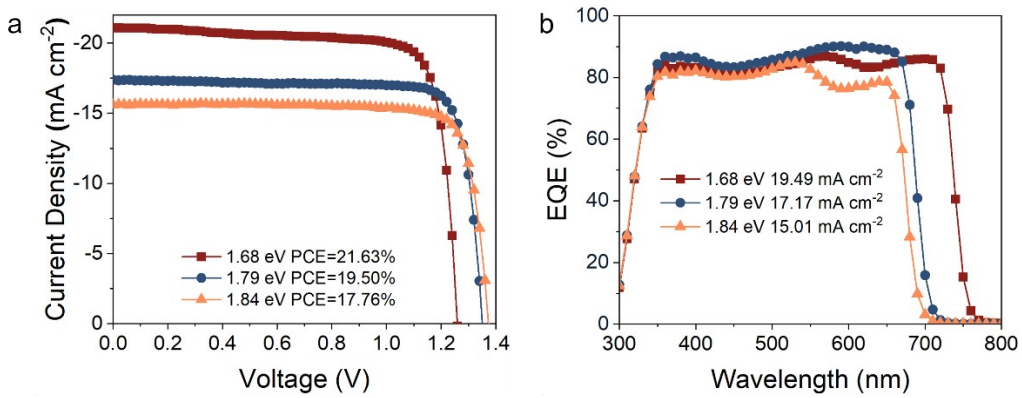

Figure S13. J-V curves (a) and EQE (b) of various bandgaps.

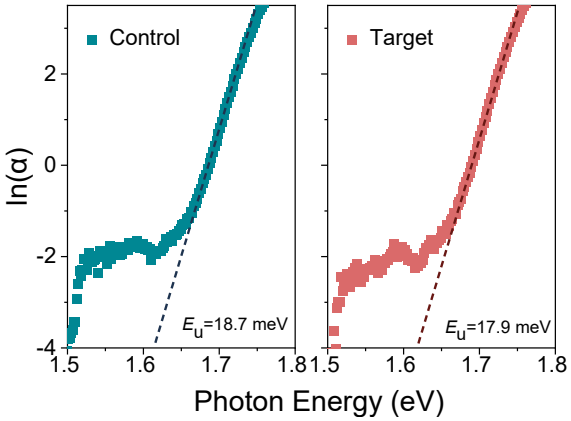

Figure S14. The logarithm of absorption coefficient versus photon energy of control and target films.

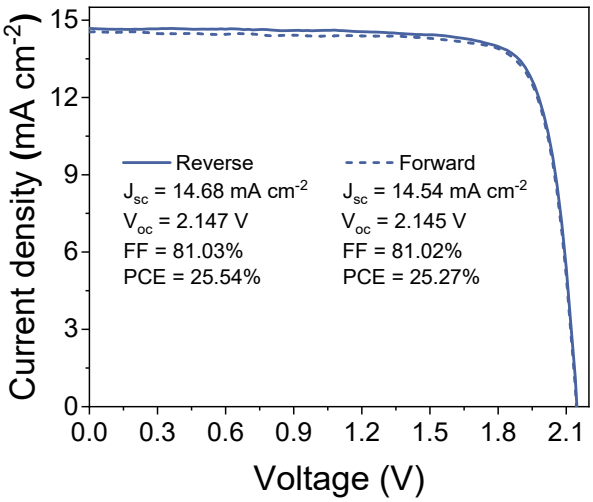

Figure S15. *J–V* curves of the best-performing tandem solar cell.

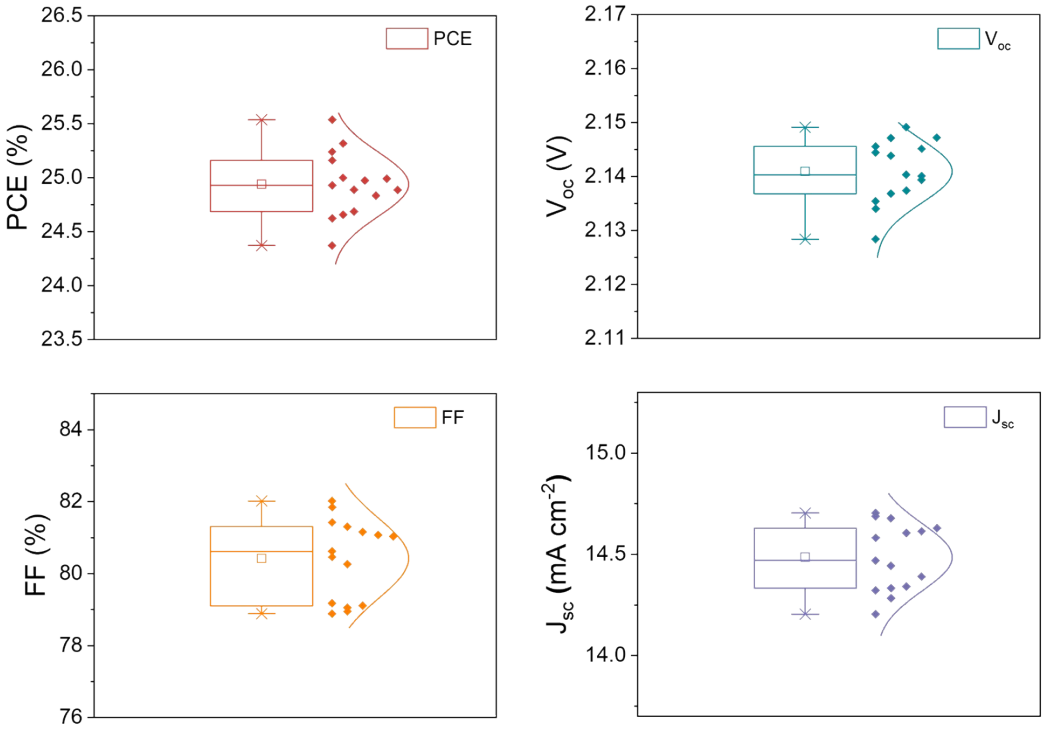

Figure S16. Statistical PCE, V_{OC}, FF, and J_{SC} of the PO-TSCs were obtained from 15 individual devices.

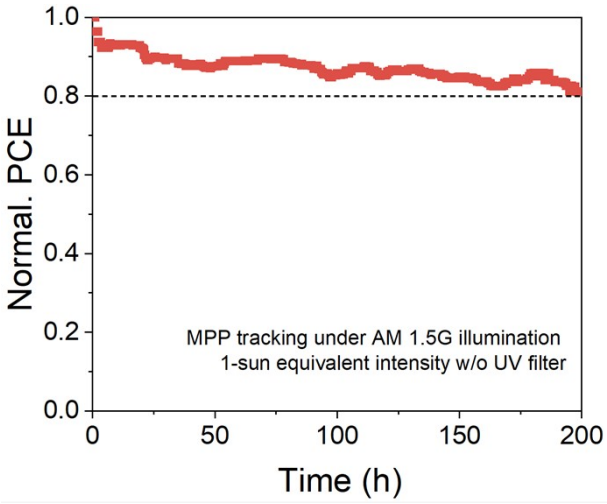

Figure S17. Long-term MPP tracking of the encapsulated TSCs under simulated AM 1.5G illumination (100 mW cm^{-2}, without UV filter) in an N_2-filled chamber without temperature control.

Supplementary Table 1. E_g and *V*oc statistics of wide-Eg perovskite solar cells.

Reference	E_g	V_{OC}
Joule 2020, 4, 1594-1606.	1.77	1.113
Nat. Energy 2020,5, 870-880.	1.77	1.206
Nat. Energy 2022, 7,229–237.	1.79	1.26
Adv. Mater. 2022, 34, 2108829.	1.79	1.25
Adv. Mater. 2022, 34, 2110356.	1.8	1.263
Nat. Energy 2022, 7,229–237.	1.79	1.26
Nature 2022, 604, 280-286.	1.85	1.34
Adv. Mater. 2022, 34, 2108829.	1.79	1.25
Adv. Mater. 2024, 2311923.	1.68	1.216
Adv. Mater. 2024, 2401103.	1.68	1.22
Nat. Sci. Rev. 2024 nwae055.	1.77	1.34
Energy Environ. Sci., 2024,17, 2512-2520.	1.78	1.25
Nature 2024, 625, 516–522.	1.77	1.3
Energy Environ. Sci., 2024,17, 1637-1644.	1.71	1.25
Adv. Funct. Mater. 2024, 2314349.	1.77	1.296
Adv. Mater. 2024, 36, 2307987.	1.66	1.27
Adv. Funct. Mater. 2023, 2312505.	1.75	1.29
Adv. Energy Mater. 2024, 14, 2302983.	1.67	1.272
Adv. Funct. Mater. 2023, 2311679.	1.68	1.2
Adv. Energy Mater. 2024, 14, 2303344.	1.65	1.24
Angew. Chem. Int. Ed. 2024, 63, e202315281.	1.68	1.215
Energy Environ. Sci., 2024,17, 202-209.	1.77	1.339

Adv. Mater. 2024, 36, 2308370.	1.67	1.262
Nat Commun. 2023,14, 7118.	1.78	1.324
Adv. Funct. Mater. 2024, 34, 2308908.	1.79	1.32
Energy Environ. Sci., 2023,16, 5992-6002.	1.78	1.35
Adv. Mater. 2023, 2306568.	1.73	1.3
	1.79	1.34
	1.85	1.36
	1.92	1.39
Adv. Funct. Mater. 2023, 33, 2300860.	1.66	1.23
Adv. Mater. 2024, 2400105.	1.67	1.25
Energy Environ. Sci., 2024 DOI: 10.1039/D4EE00330F	1.68	1.256
Small Methods 2024, 2400067.	1.7	1.24
	1.68	1.193
Adv. Mater. 2023, 35, 2305946.	1.85	1.35
Adv. Mater. 2024, 36, 2307743.	1.8	1.34
Science 2022, 378, 1295-1300.	1.75	1.33
Nature 2023 613, 676-681.	1.79	1.33
Nature 2023, 618, 80-86.	1.77	1.31
Nat. Energy 2024, 9, 411–421.	1.81	1.351
Nat. Energy 2024, 9, 592–601.	1.83	1.32
Science 2024, 384,767-775.	1.77	1.35
This work	**1.79**	**1.35**

Supplementary Table 2 V_{OC} and PCE statistics of reported perovskite-organic TSCs.

Reference	Wide-E_g	V_{OC}	PCE
Joule 2020, 4, 1594	1.77	1.902	20.6
Adv. Sci. 2022, 9, 2200445	1.92	2.097	20.6
Nano Lett. 2021, 21, 7845	1.92	1.96	21.1
Adv. Funct. Mater. 2022, 32, 2112126	1.72	1.96	21.2
J. Mater. Chem. A 2023, 11, 6877	1.71	2.06	21.3
Nano Today 2022, 46, 101586	1.9	2.22	21.4
Adv. Mater. 2022, 34, 2108829	1.79	1.88	22.01
Small 2022, 18, 2204081	1.79	2.072	22.29
Adv. Funct. Mater. 2023, 33, 2212599	1.9	2.095	22.43
Adv. Mater. 2023, 35, 2208604	1.91	2.15	23.17
Adv. Energy Mater. 2023, 13, 2204347	1.9	2.1	23.21
Nat. Energy 2022, 7, 229	1.79	2.063	23.6
Nature 2022, 604, 280	1.85	2.15	24
Adv. Mater. 35, 2305946-202342	1.85	2.14	24.47
Adv. Mater. 2023, 2306568.	1.85	2.197	24.12
Chin. J. Chem. 2024, https://doi.org/10.1002/cjoc.202400071	1.83	2.11	24.05
Adv. Mater. 2024, 2312704.	1.77	2.09	24.33
Nat. Energy 2024, 9, 411–421.	1.81	2.151	25.22
Nat. Energy 2024. 9, 592–601.	1.83	2.12	25.82
This work	**1.79**	**2.147**	**25.54**

Supplementary Table 3. Corresponding device parameters of IA different doping concentrations.

Concentration (mol%)	V_{OC} (V)	J_{SC} (mA cm^{-2})	*FF* (%)	PCE (%)
1	1.34	17.16	82.95	19.22
2	1.35	17.39	83.07	19.50
3	1.32	17.71	81.27	18.97
4	1.32	17.59	80.85	18.81

Supplementary Table 4. Device parameters of various bandgaps.

Bandgap (eV)	V_{OC} (V)	J_{SC} (mA cm^{-2})	*FF* (%)	PCE (%)
1.68	1.26	21.10	80.35	21.36
1.79	1.35	17.39	83.07	19.50
1.84	1.37	15.58	82.97	17.69

References

1 Q. Cheng, B. Wang, G. Huang, Y. Li, X. Li, J. Chen, S. Yue, K. Li, H. Zhang, Y. Zhang and H. Zhou, *Angew Chem Int Ed*, 2022, **61**, 134, e202208264.

2 M. Chen, X. Dong, Y. Xin, Y. Gao, Q. Fu, R. Wang, Z. Xu, Y. Chen and Y. Liu, *Angew Chem Int Ed*, 2024, **63**, e202315943.

3 S. Wu, J. Zhang, Z. Li, D. Liu, M. Qin, S. H. Cheung, X. Lu, D. Lei, S. K. So, Z. Zhu and Alex. K.-Y. Jen, *Joule*, 2020, **4**, 1248–1262.